

CFD and CHA simulation of underwater noise induced by a marine propeller in two-phase flows

Ville M. Viitanen,¹ Antti Hynninen,¹ Lars Lübke,² Rhena Klose,² Jukka Tanttari,¹
Tuomas Sipilä,¹ Timo Siikonen^{3,4}

¹VTT Technical Research Centre of Finland Ltd.

²SVA, Potsdam Model Basin, Germany

³FINFLO Ltd., Espoo, Finland

⁴Department of Mechanical Engineering, Aalto University, Espoo, Finland

ABSTRACT

A propeller in uniform homogeneous inflow is studied numerically utilizing computational fluid dynamics (CFD) and computational hydroacoustics (CHA). The investigations are performed at one propeller loading in wetted and cavitating conditions. The turbulence is modelled with Chien's $k - \varepsilon$ model and Menter's SST $k - \omega$ with Explicit Algebraic Reynolds Stress Model (EARSM). The corresponding induced harmonic and broadband noise from the propeller are investigated numerically. The influence of the sheet and tip vortex cavitation and the employed turbulence modelling to the induced noise are studied.

In this paper, the Potsdam Propeller Test Case (PPTC) propeller (Barkmann *et al.*, 2011) is investigated. The propeller is operating in push configuration. The performance of the propeller in terms of global forces is compared with the model tests. The cavitation extents are compared with the observations made in model scale tests carried out in a cavitation tunnel.

The global performance of the propeller is captured well in wetted and cavitating conditions. A good agreement has been achieved between the simulated and experimentally observed cavitation patterns, especially in the wake of the propeller. The cavitating tip vortex is captured exceptionally well in the simulations. The predicted noise emissions seem reasonable, and effects due to different turbulence closures or due to cavitation are recognized. Validation of the present acoustic simulations with experimental results is still needed.

Keywords

Marine propeller, Hydroacoustics, Cavitation, Turbulence modelling

1 INTRODUCTION

The growing global shipping rates generate increasing acoustic output to the underwater environment. The deep-ocean noise levels have grown over the past four decades, which correlates with the observed increase in global shipping rates (Andrew *et al.*, 2002). In addition, the adverse effects of shipping noise on marine mammals became of concern in the 1970s when the overlap between the main frequencies

used by large baleen whales and the dominant components of noise from ships was noted (Payne & Webb, 1971). The fish have also been observed to be disturbed by ship emitted noise (Mitson, 1995). The sound emitted from naval and research vessels and submarines can interfere with the measurement equipment, or be used for detection. The noise emitting into the interior of the ship may disturb the crew and the passengers on board and increase hull vibration levels. The noise emission levels are important especially for cruise liners and yachts from the comfort and ship mission points of view.

Marine propellers are important source of noise emitted from ships to the underwater environment and to the interior of the vessel. A non-cavitating propeller induces discrete peaks to the noise spectrum, which occur at the blade passing frequency and its multiples. These peaks are related to blade thickness and loading induced pressure pulses. In addition, a propeller induces broadband noise, which is related to unsteadiness in the flow field. This corresponds to the turbulent fluctuations in the velocity and pressure fields. In the case of phase changes, the underwater noise from cavitation dominates other propeller induced noise, excluding singing, and all other underwater noise from a ship (Lightelijn, 2007). Sheet and tip vortex cavitation usually increase the amplitude of the tonal pressure fluctuations. Unsteady cavitation structures give rise to propeller induced broadband signature.

During the past decade, CFD has been actively utilized to study the propeller performance in wetted and cavitating conditions (Balaras *et al.*, 2015; Lu *et al.*, 2014; Muscari *et al.*, 2013; Sipilä *et al.*, 2009; Turunen *et al.*, 2014). Flow structures in the wake and tip vortex of a propeller employing different RANS (Reynolds-averaged Navier-Stokes) or scale-resolving turbulence closures have been studied by Sipilä *et al.* (2014) and Guilmineau *et al.* (2015). Additionally higher fidelity turbulence closures, such as the LES or DES (large eddy simulation or detached eddy simulation, respectively) approach have been used to compute the flow past marine propellers for instance by Lu *et al.* (2014), Muscari *et al.* (2013), Chase & Carrica (2013) and Balaras *et al.* (2015). Specific attention towards the peculiar nuisance of propeller induced noise has been given, *e.g.*, by Ianniello *et al.* (2013), Lloyd *et al.*

(2015) and Lidtke *et al.* (2015) via a utilization of the Ffowcs Williams-Hawkings acoustic analogy. Budich *et al.* (2015) studied the PPTC propeller in cavitating conditions, where the authors focused on the shock wave dynamics including an erosion assessment.

In this paper, the propeller in uniform homogeneous inflow condition is studied numerically utilizing CFD and CHA. The combined hydrodynamic-hydroacoustic problem is solved via a hybrid approach. In the hybrid method, the flow solution consisting of a URANS (unsteady RANS) computation is assumed to be decoupled from the acoustic propagation, which is comprised of an acoustic finite element (AFEM) computation. The effective assumption is that the acoustic field does not modify the bulk flow solution. Consequently, the flow problem is solved independently and prior to the solution of the acoustic problem.

The flow simulations have been conducted with the general purpose CFD solver FINFLO (Sipilä *et al.*, 2009; Sánchez-Caja *et al.*, 1999). The code has been applied to both cavitating and non-cavitating propeller flows (Sipilä *et al.*, 2014; Viitanen *et al.*, 2015). The propeller induced sound pressure levels are obtained using ACTRAN (Free Field Technologies SA, 2015). The investigations are performed at one propeller operation point in wetted and cavitating conditions. The corresponding induced harmonic and broadband noise from the propeller are investigated. The influence of sheet and tip vortex cavitation, as well as the employed turbulence modelling, to the harmonic and broadband noise are studied.

2 COMPUTATIONAL CASE

The investigated PPTC propeller is a model-size propeller with a diameter of 0.250 m. The five-bladed propeller has a right-handed direction of rotation. The skew of the propeller is moderate. Tab. 1 summarizes the main geometrical parameters of the PPTC propeller. A photograph of the propeller is shown in Fig. 1. In this study, the propeller is operating in push configuration. Large database of experimental results has been made available by SVA Potsdam¹.

A single propeller point of operation, both in wetted and cavitating conditions, is considered. The simulations have been performed using a constant rate of revolutions, $n = 20$ 1/s. The advance coefficient and cavitation number are defined as

$$J = \frac{V_A}{nD} \quad \text{and} \quad \sigma_n = \frac{p - p_{\text{sat}}}{\frac{1}{2}\rho(nD)^2}, \quad (1)$$

respectively, where V_A is the propeller speed of advance, n the propeller rate of revolutions and D the propeller diameter, p is the pressure, p_{sat} the saturation pressure and ρ the fluid density. The investigated condition is $J = 1.019$ and $\sigma_n = 2.024$. This corresponds to the PPTC Case 2.3.1 of smp'11 Workshop (Barkmann *et al.*, 2011). The thrust and

torque of the propeller are non-dimensionalized as

$$K_T = \frac{T}{\rho n^2 D^4} \quad \text{and} \quad K_Q = \frac{Q}{\rho n^2 D^5}, \quad (2)$$

respectively, where T denotes the thrust and Q the torque of the propeller.

Table 1: Main geometric parameters of the PPTC propeller.

Diameter [m]	0.250
Pitch ratio at $r/R = 0.7$	1.635
Chord at $r/R = 0.7$	0.417
EAR	0.779
Skew [°]	18.837
Hub ratio	0.300
Number of blades	5
Rotation	Right handed



Figure 1: PPTC propeller.

3 CAVITATION TEST

In course of the investigations for the smp'11 and smp'15 propeller workshop and various research projects the VP1304 propeller was remanufactured as fixed pitch propeller P1790 and retested in different conditions. Due to progress in the manufacturing process it was possible to achieve a higher accuracy, especially concerning the leading edge shape, for the remanufactured propeller. This leads to small differences in the cavitation pattern between the two propellers (VP1304 and P1790), while the integral values such as thrust and torque remain unchanged. The differences in cavitation pattern were only observed for the advance coefficient of $J = 1.019$, for which also a high sensitivity regarding the oxygen saturation could be detected.

Fig. 2 shows the observed cavitation patterns on the suction side of the blade with the highest tested oxygen saturation rate. Streak cavitation at the leading edge occurred differently on all blades.

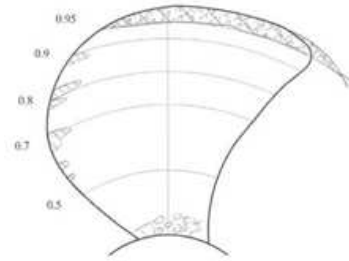


Figure 2: Cavitation observation for P1790 propeller for oxygen saturation of $\alpha/\alpha_s = 61.3\%$.

4 NUMERICAL METHOD

4.1 CFD solution

The equations are solved using a SIMPLE type pressure correction method (Miettinen & Siikonen, 2015). The inviscid

¹<http://www.sva-potsdam.de/pptc-smp11-workshop/>

fluxes are evaluated using a Rhie-Chow type dissipation in the convective part. The variables are interpolated onto the cell surfaces using a MUSCL interpolation (Van Leer, 1979). In this study usually a third-order upwind-biased scheme is applied. For the gas continuity equation, however, limiters are applied. The diffusive fluxes as well as the pressure gradients are centrally differenced. The three-level fully implicit method is used in the time-accurate cases. An algebraic multi-grid method (AMG) with line Gauss-Seidel smoothing is employed to solve the pressure correction equation.

Two different solution strategies are utilized for the simulations of the flow around the rotating propeller. The first one is to rotate the computational domain with the propeller rate of revolution, and integrate the governing equations in the physical time. Consequently, CFD results which yield from this strategy are referred to as transient. In this approach, a steady-state solution is sought within each physical time step, and the equations are iterated until the L_2 norms of the main variables have decreased by a sufficient amount, *i.e.*, at least 2-3 orders of magnitude. One hundred inner iterations were required within each physical time step for the wetted simulations, and approximately 125 inner iterations were required for the cavitating simulations. Physical time-step of $\Delta t_{CFD} = 0.139$ ms is used, corresponding to 1° of propeller rotation. The second approach exploits the fact that the governing equations can yield a steady-state solution, when the equations are expressed in the coordinate system that is rotating with the propeller. Consequently, this solution method is referred to as quasi-steady. Absolute velocities are used in the solution, and the rotational movement of the propeller is accounted for in the convection velocity and as source terms in the y and z -momentum equations as the propeller is rotating around the x -axis. The equations are iterated until the global force coefficients and the L_2 norms of the main variables have obtained a sufficiently steady level, with the L_2 norms having decreased to $10^{-5} \dots 10^{-7}$. Utilizing the quasi-steady approach, the ‘time-dependent’ data for the acoustic analyses is produced by subsequent artificial rotation of the flow solution around the rotation axis. The chosen time-step for the rotated quasi-steady data corresponds to 1° of propeller rotation.

For the two-phase simulations, a homogeneous mixture model is employed. The flow is assumed isothermal, which decouples the energy equation from the system. Both phases share the same velocity, which simplifies the modelling, especially in the case of turbulence models. The turbulence modeling is applied for the mixture. Furthermore, a single-pressure system is employed. In the code, the continuity equation for the gas and liquid phase separately, and the momentum equations for the mixture are solved. The system of equations is in differential form

$$\frac{\partial \rho}{\partial t} + \frac{\partial \rho u_i}{\partial x_i} = 0, \quad (3)$$

$$\frac{\partial \rho u_i}{\partial t} + \frac{\partial \rho u_i u_j}{\partial x_j} = -\frac{\partial p}{\partial x_i} + \frac{\partial \tau_{ij}}{\partial x_j}, \quad \text{and} \quad (4)$$

$$\frac{\partial \alpha \rho_g}{\partial t} + \frac{\partial \alpha \rho_g u_i}{\partial x_i} = -\Gamma, \quad (5)$$

where ρ is the density of the mixture, u_i the velocity field of the mixture, p is the pressure, τ_{ij} the viscous stress tensor, α the gas volume fraction, ρ_g the density of the gas phase, and Γ is the mass transfer term. Note that in a two-phase system the liquid volume fraction follows from that of the gas phase as $\alpha_l = 1 - \alpha$.

4.1.1 Turbulence modelling

The turbulence models applied in the present calculations are the low Reynolds number $k - \varepsilon$ model of Chien (1982), and the SST $k - \omega$ of Menter (1994). The latter formulation is used in connection with the explicit algebraic Reynolds stress model (EARSM) of Wallin & Johansson (2000). The calculations were performed up to the wall, and the turbulence modeling was applied for the mixture. The non-dimensional wall distance was adjusted such that $y^+ \approx 1$ for the first cell. The SST $k - \omega$ is a zonal model, referring to the formulation where the $k - \omega$ equations are solved only inside the boundary layer, and the standard $k - \varepsilon$ equations, transformed to the ω -formulation, are solved away from the walls.

Both the $k - \varepsilon$ and the $k - \omega$ turbulence models are isotropic, *i.e.*, they predict the Reynolds stress tensor according to the Boussinesq approximation. In other words, no individual modelling is employed for each normal turbulent stresses; only their sum, $k = \overline{u_i' u_i'}/2$, is modelled. To account for turbulent anisotropy, the EARSM can be utilized. The idea in algebraic Reynolds stress models is to allow a non-linear relationship between the rate of mean strain and the Reynolds stresses, but without the need of solving additional partial differential equations for each of the six Reynolds stresses. The EARSM relies on either of the two-equation formulation but with the Reynolds stress anisotropy tensor evaluated from a linear pressure-strain model, and forms a physically well-founded strategy among two-equation models for improved prediction of flows involving complex features such as streamline curvature effects and system rotation (Hellsten & Laine, 2000).

4.1.2 Cavitation modelling

In the homogeneous mixture model, the mass transfer term between the liquid and gaseous phases, Γ , is modelled. In this study, the mass transfer model similar to that of Merkle *et al.* (1998) is utilized. In the model, the liquid phase begins to vaporize as the local pressure drops below the saturation pressure. Similarly, the vapour phase begins to condensate as the local pressure rises above the saturation pressure. The saturation pressure is found from the Antoine equation

$$\log(p_{sat}) = A - \frac{B}{T_{sat} + C}, \quad (6)$$

where the parameters A , B and C are obtained empirically, and T_{sat} is the saturation temperature (Lindstrom & Mallard, 2005; Siikonen, 2009). In the utilized model, the mass transfer

is evaluated from

$$\Gamma = \frac{C_{dest} \rho_l \alpha_l \min(0, p - p_{sat})}{1/2 \rho_\infty V_\infty^2 (L_{ref}/V_{ref})} + \frac{C_{prod} \rho_g \alpha_g \max(0, p - p_{sat})}{1/2 \rho_\infty V_\infty^2 (L_{ref}/V_{ref})}, \quad (7)$$

where $C_{dest} = 350$ 1/s and $C_{prod} = 350$ 1/s were chosen as the empirical parameters for the cavitation model (see Sipilä (2012) for details). In Eq. (7) ρ_l is the density of the liquid phase, α_l is the volume fraction of the liquid phase, ρ_g is the density of the gas phase and α_g is the volume fraction of the gas phase. ρ_∞ and V_∞ are the free stream density and velocity, respectively. V_{ref} and L_{ref} are the reference velocity and length, respectively.

In all cavitating simulations where the non-linear two-equation turbulence model is employed, a third-order accurate upwind-biased interpolation with TVD SUPERBEE limiter of Roe (1985) is utilized for the convection terms in the void fraction equation. In all cavitating simulations where Chien's $k - \varepsilon$ turbulence model is employed, a second-order accurate upwind interpolation with TVD limiter of van Albada *et al.* (1982) is utilized for the convection terms in the void fraction equation.

4.1.3 Grid and boundary conditions

The propeller is operated in push configuration, *i.e.*, the shaft is located in front of the propeller. The used computational grid consists of roughly 5.5 million cells in 28 grid blocks. The surface grid on the suction side of the blade is shown in Fig. 3(a). The surface grid on the pressure side of the blade is similar. The grid has an O-O topology around the propeller blades. The grid resolution around the leading edge is fine as is shown in Fig. 3(b), and there are about 30 cells around the leading edge radius. Due to the O-O topology, the same resolution is applied around the blade tip and the trailing edge as well. The grid is refined normal to the viscous surfaces such that $y^+ \approx 1$.

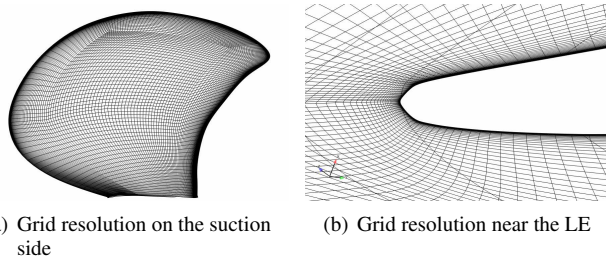


Figure 3: Grid resolution on the suction side and near the leading edge of the blade.

The calculations were performed on three grid levels. At a coarser grid level, every second point in all directions is taken into account compared to a finer level grid. The computations on a coarser grid are used as the initial guess for the computations performed on a finer grid level. In this paper, we present

the results that were obtained on the finest grid.

The computational domain is shown in Fig. 4. Due to the symmetric nature of the problem of a propeller operating in uniform inflow, only one blade is modeled. The inlet is located five propeller diameters upstream of the propeller, and the outlet is located ten diameters downstream of the propeller. The rectangular cavitation tunnel of SVA Potsdam was here modeled as a circular duct of the same cross-sectional area, thus enabling the quasi-steady computation of the problem. The radius of the computational domain is then 0.3385 m.

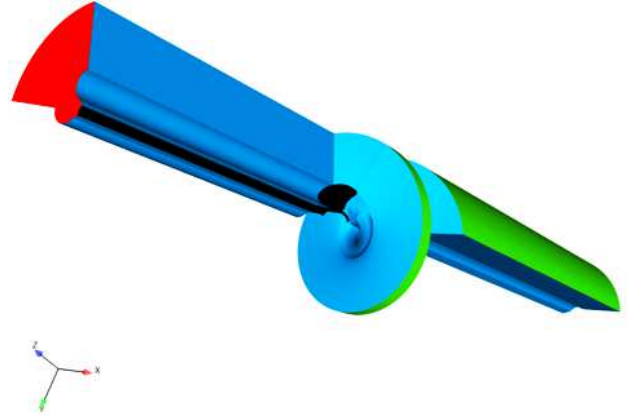


Figure 4: Perspective view of the computational domain utilized in the calculations. The propeller, hub and shaft are coloured with black. The inlet face is coloured with red. The cyclic boundaries are colored with blue, and the simplified tunnel wall is colored with green.

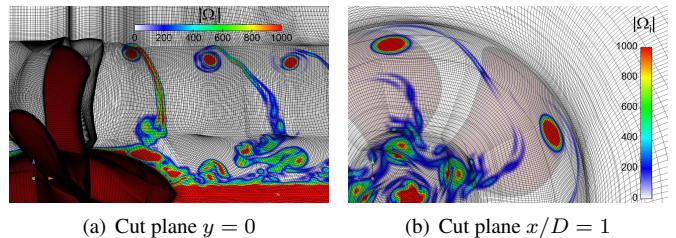


Figure 5: Views of the cut plane $y = 0$, and the cut plane $x/D = 1$, showing the fine grid at these planes. $|\Omega_i|$ denotes the absolute value of vorticity. The propeller blades, hub and shaft are colored with dark red.

The grid points in the helical blocks located downstream of the propeller were concentrated in the region of the tip vortex. Fig. 5 depicts the concentration of the grid points near the tip vortex induced by the rotating blades. The figure shows exemplary views of the resolution on the finest grid, demonstrating that the tip vortex is excellently maintained even beyond $x/D \approx 1$. There are roughly 18×14 grid points in the cross-section of the tip vortex on the finest grid on the plane $x/D = 1$. The helical blocks in the slipstream of the propeller are extended to a pitch corresponding approximately to 450° of rotation

from the propeller plane.

The blades, hub and shaft are modeled as no-slip rotational surfaces. A velocity boundary condition is applied at the inlet, and a pressure boundary condition is applied at the outlet. Slip boundary condition is applied at the simplified tunnel walls. The whole computational domain is considered as rotating with the given rate of rotation. The inflow velocity is set based on the advance numbers of the propeller, and the background pressure level is set to either a large value for the wetted flow simulations, $\mathcal{O}(10^6)$, or set based on the cavitation number in the cavitating case.

4.2 CHA solution

Instead of the direct solution of the compressible Navier-Stokes equations, the hydrodynamic and hydroacoustic problems are treated separately. The former is considered as an incompressible solution to Eqs. (3 - 4), while the latter can be seen as a subsequent solution of the compressible Navier-Stokes equations in isentropic conditions. The acoustic problem is analogous to a direct solution in the sense that the flow generated noise propagates not through the mean flow, but according to a wave operator in a medium at rest. In this analogous problem, source terms are utilized to represent the flow. The effectively two-step approach requires one unsteady flow solution in time domain and one subsequent acoustic analysis in the frequency domain.

The present solution to the acoustic problem is based on the acoustic analogy using the ACTRAN code (Free Field Technologies SA, 2015). The propagation problem, in which noise is generated by small flow fluctuations, is replaced by an analogous problem, where the propagation is represented by a wave operator. In this study, the Lighthill (1952) analogy is used, which utilizes a wave equation for density. The wave equation can be derived by taking the time-derivative of the continuity equation, and the gradient of the momentum equations. Combining these two yields

$$\frac{\partial^2 \rho}{\partial t^2} - c_0^2 \frac{\partial^2 \rho}{\partial x_i^2} = \frac{\partial^2 T_{ij}}{\partial x_i \partial x_j}, \quad (8)$$

where c_0 is the speed of sound of the medium, and $T_{ij} = \rho u_i u_j + (p - c_0^2 \rho) \delta_{ij} + \tau_{ij}$ the Lighthill tensor. Furthermore, T_{ij} can be simplified by assuming isentropic, high- Re and low- Ma flows to comprise only of the fluid momentum components, or $T_{ij} \approx \rho u_i u_j$. The wave equation can be transformed to the frequency domain

$$-\omega^2 \tilde{\rho} - c_0^2 \frac{\partial^2 \tilde{\rho}}{\partial x_i^2} = \frac{\partial^2 \tilde{T}_{ij}}{\partial x_i \partial x_j}, \quad (9)$$

where ω is the angular frequency. In ACTRAN, the solution of the acoustic problem, Eq. (8), is based on variational formulation of the wave equation for density propagation, transformed into the frequency domain, Eq. (9). The code requires the Lighthill tensor in the frequency domain as an input. The source terms $\nabla \cdot (\nabla \cdot \tilde{T}_{ij})$ are related solely to the momentum components, which are provided by the flow solution.

4.2.1 Methodology

In ACTRAN, instead of the density a transformed potential, ψ , defined through

$$\tilde{\rho} = -\frac{i\omega\psi}{c_0^2} \quad (10)$$

is used. The alternative equation for the Lighthill analogy is then

$$\frac{\omega^2}{c_0^2} \psi + \frac{\partial^2 \psi}{\partial x_i \partial x_i} = \frac{1}{i\omega} \frac{\partial^2 \tilde{T}_{ij}}{\partial x_i \partial x_i}. \quad (11)$$

The weak variational formulation for the density propagation in the frequency domain involving stationary and moving geometry reads

$$\begin{aligned} & - \int_{\Omega} \frac{\omega^2}{\rho_0 c_0^2} \psi \delta \psi d\Omega - \int_{\Omega} \frac{1}{\rho_0} \frac{\partial \psi}{\partial x_i} \frac{\partial \delta \psi}{\partial x_i} d\Omega \\ & = \int_{\Omega} \frac{1}{\rho_0 \omega} \frac{\partial \delta \psi}{\partial x_i} \frac{\partial T_{ij}}{\partial x_j} d\Omega - \int_{\Gamma} \frac{1}{\rho_0} \mathcal{F}(\tilde{\rho} \tilde{v}_i n_i) d\Gamma. \end{aligned} \quad (12)$$

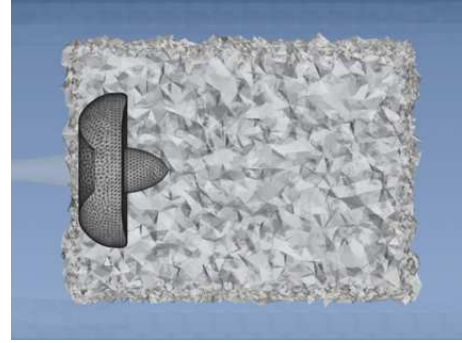


Figure 6: Lighthill surface mesh around the propeller blades and hub, and Lighthill volume mesh around the propeller, and in the wake of the propeller.

Two types of source terms are present in Eq. (12). The surface source terms are evaluated on the surface surrounding the propeller blades and hub. Conformal surface enclosing the propeller blades is shown in Fig. 6. The noise generation resulting from flow phenomena such as turbulence, blade loading and cavitation, take place inside the volume surrounding the blades and the hub, shown in Fig. 6. It is accounted for by mapping the sources as defined in Eq. (12) onto the enclosing surface. In practice, in order to achieve the most accurate source description, the surface should be located close to the source, *i.e.*, the unsteady flow. The volume mesh encloses the propeller and the wake region as shown in Fig. 6, and the volume source terms in Eq. (12) are evaluated in these volume elements. The hydroacoustic source terms are calculated in time domain using oversampling by default at every half CFD time steps to avoid aliasing effects during the Fourier transform, and saved in an NFF database. The calculated hydroacoustic source terms are then transformed on the acoustic mesh by integrating over the CFD mesh using the shape functions of the acoustic mesh.

4.2.2 Grid and boundary conditions

The acoustic FE mesh is shown in Fig. 7. The maximum frequency that can be resolved within the acoustic analyses is limited by the Nyquist frequency and the time step used in the transient CFD computations, *i.e.*, $f_{max} = 0.5/\Delta t_{cfd} = 3.6$ kHz. The lowest frequency that can be resolved, $f_{min} = 20$ Hz, is set by the physical simulation time, which in this case is one propeller revolution. There are more than six elements for the shortest wave length. In total, there are 450 000 quadratic tetrahedron elements in the mesh. At both ends of the cavitation tunnel, non-reflecting boundary conditions are used. The tunnel walls are modeled as rigid.

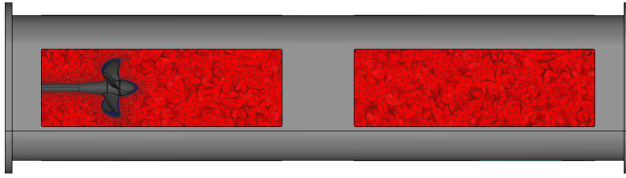


Figure 7: Acoustic FE mesh inside the cavitation tunnel.

5 RESULTS

Results for wetted and cavitating simulations are presented below. Unless otherwise stated, all CFD results shown are obtained using the transient approach. In all figures depicting the CFD results, the blade is at the top-dead center. Transient simulations in wetted and cavitating conditions were conducted with the $k - \varepsilon$ and the SST $k - \omega$ EARSM turbulence models. Quasi-steady CFD simulations were conducted utilizing the $k - \varepsilon$ model both for the wetted and cavitating conditions.

5.1 Global performance characteristics

The comparison of the simulated results with the cavitation tunnel tests in terms of the non-dimensional thrust and torque coefficients is given in Tab. 2 for the wetted and cavitating conditions. It is seen that the propeller performance in terms of global forces is captured well in both wetted and cavitating conditions. The differences are within few percent for all investigated operation points.

Table 2: Comparison of the global forces in wetted and cavitating conditions. CFD results are obtained using the fine grid.

	K_T	ΔK_T	$10K_Q$	ΔK_Q
EFD, wett.	0.387	-	0.975	-
CFD, wett.	0.384	-0.8 %	0.976	0.1 %
EFD, cav.	0.374	-	0.970	-
CFD, cav.	0.368	-1.6 %	0.947	-2.4 %

Tab. 2 shows results obtained with the $k - \varepsilon$ turbulence model using the transient approach. Corresponding differences with quasi-steady computations were $\Delta K_T = -0.4\%$ and $\Delta K_Q = -1.6\%$ at wetted conditions, and $\Delta K_T = -1.6\%$

and $\Delta K_Q = -2.0\%$ at cavitating conditions. The differences of the corresponding transient results obtained with the SST $k - \omega$ EARSM were within 5 per cent for the thrust and torque coefficient.

5.2 Cavitation observation

The cavitation patterns on the suction side of the propeller blades are compared with the observations made in the cavitation tunnel tests in Figs. 8 and 9. The propeller has strong tip vortex and hub vortex cavitation, which are visible in the experiments and in the simulations. Shedding of root cavitation was observed in the experiments and in the simulations. The unstable behaviour was very mild in the simulations. Otherwise, the mean shape and extent of the root cavitation, as well as the tip and hub vortex cavitation, are captured well. The tip and hub vortex cavitation extending far behind the propeller are captured exceptionally well, as shown in Fig. 9. Comparing the EFD and CFD results in Fig. 9, also the modal shapes of the cavitating tip vortex are qualitatively well captured. Streak cavitation was observed in the experiments at several radial locations near the leading edge of the blade, while the simulation predicts sheet cavitation at the leading edge.

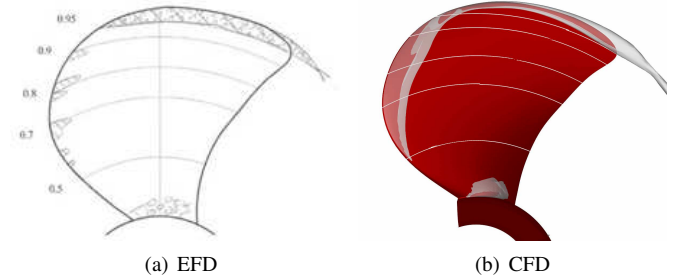
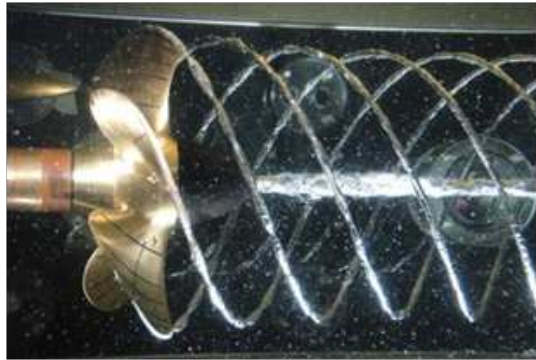


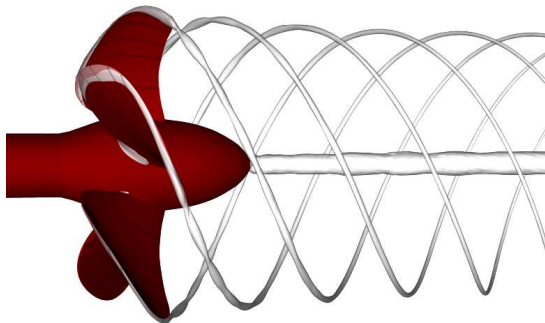
Figure 8: Comparison of the cavitation patterns near the blade surfaces with the cavitation sketches according to observations made in the experiments. In the simulated results, the grey transparent surface denotes the iso-surface of $\alpha = 0.1$. Results are obtained with SST $k - \omega$ EARSM.

Surface restricted streamlines and non-dimensional pressure coefficients, $C_p = \frac{P_{dif}}{0.5\rho_\infty(nD)^2}$, on the blade surface, predicted by the different turbulence models in wetted and cavitating conditions, are shown in Fig. 10. In all simulated wetted cases the boundary layer flow is mostly circumferentially directed with no apparent separation regions. The surface pressure distributions in the wetted conditions are similar between the two utilized turbulence models. The effect of cavitation on the surface restricted streamlines is significant. The re-entrant jets are directed towards the cavitating tip vortex at the closure line of the sheet cavitation. Similar phenomenon was observed by Sipilä (2012), see also Fig. 14. This behaviour appears as nearly identical for both of the utilized turbulence models. In addition, apparent flow separation is observed in the blade root region at cavitating conditions. When utilizing the non-

linear model, the region of separating flow extends to slightly higher radii near the trailing edge than for the $k - \varepsilon$ model.



(a) EFD



(b) CFD

Figure 9: Tip and hub vortex cavitation extents behind the propeller. In the computed result, the grey transparent surface denotes the iso-surface of $\alpha = 0.1$. CFD results are obtained with SST $k - \omega$ EARSM.

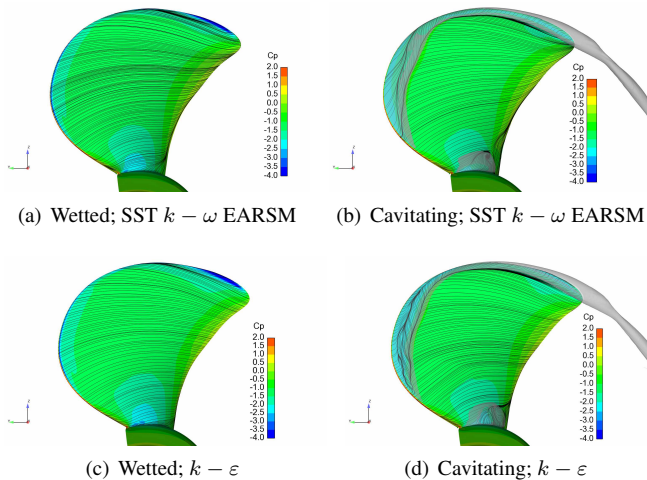
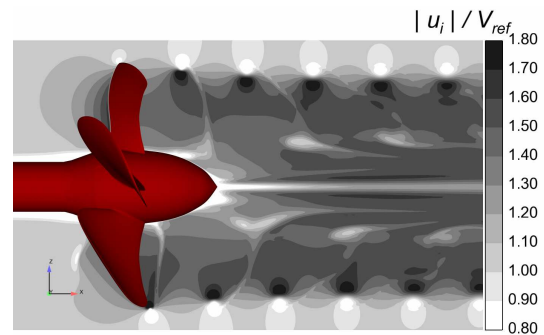


Figure 10: Surface restricted streamlines and non-dimensional pressure coefficients on the blade surface. Wetted and cavitating conditions utilizing different turbulence models. The grey transparent surface in the cavitating simulations denotes the iso-surface of $\alpha = 0.1$.

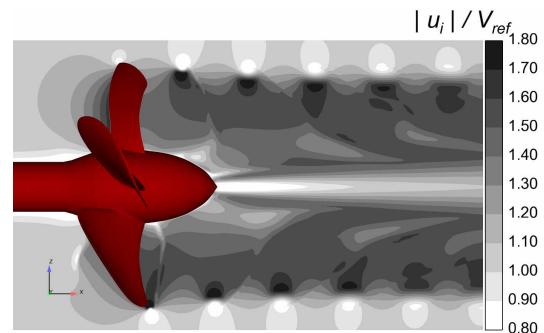
Otherwise, the effects of the turbulence model on the surface restricted streamlines and the cavitation patterns in the vicinity of the blades appears as minor. In cavitating conditions, the surface pressure distributions are mostly similar, except for the separation region near the blade root.

5.3 Flow structures and turbulence quantities behind the propeller

The magnitude of non-dimensional velocity ($V_{ref} = V_A$) behind the propeller in wetted conditions is shown in Fig. 11. In the figure, the results obtained utilizing the different turbulence models are visualized. It is seen that the strong tip vortex is preserved well in the slipstream. Especially when using the non-linear model, the disturbance at the tip vortex region is convected far in the wake, nearly unaffected by the distance it has travelled. In the case of the $k - \varepsilon$ model, there is more dissipation visible in the tip vortex region. Moreover, the overall flow features in the wake of the propeller seem less pronounced, when utilizing the $k - \varepsilon$ turbulence model. The apparent flow separation near the trailing edge of the propeller hub causes visible disturbances, which again are more pronounced in the results obtained with the non-linear model. The decelerated flow region in the innermost radii in the slipstream behind the hub is notably narrower, but still rather regular, in the results obtained with the SST $k - \omega$ EARSM.



(a) SST $k - \omega$ EARSM



(b) $k - \varepsilon$

Figure 11: Magnitude of the non-dimensional velocity on the cut plane $y = 0$ in wetted conditions.

The magnitude of non-dimensional velocity behind the propeller in cavitating conditions is shown in Fig. 12. In the figure, the results obtained utilizing the different turbulence models are visualized. As was the case with the wetted computations in Fig. 11, the strong tip vortex is preserved well in the slipstream also in cavitating conditions. Especially utilizing the non-linear model, the cavitating tip vortex is preserved up to the extent of the helical grid. The pressure in the tip vortex region predicted by the $k - \varepsilon$ model, which is not shown here, decreases in magnitude at around the extent of the propeller hub, causing the vapour to vanish far sooner than in the case of the SST $k - \omega$ EARSM. The disturbance at the tip vortex region is convected nearly unaffected by the distance it has travelled when utilizing the non-linear turbulence model. Dissipation of flow disturbances in the cavitating tip vortex region is higher with the $k - \varepsilon$ model. It is observed that when employing the $k - \varepsilon$ turbulence model, the overall flow field in the wake appears rather smooth, similarly as was seen the wetted conditions. The apparent flow separation near the propeller root causes visible disturbances, which are significantly more pronounced in the results obtained with the non-linear model.

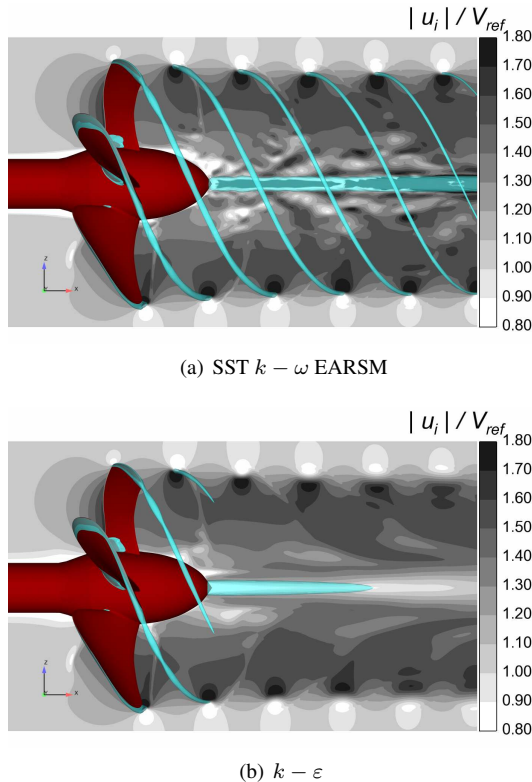


Figure 12: Magnitude of the non-dimensional velocity on the cut plane $y = 0$ in cavitating conditions. The transparent iso-surface of the void fraction $\alpha = 0.1$ is colored by blue.

Fig. 13 show a comparison of the eddy viscosity between different turbulence models. The comparison is done for the cavitating conditions. In the cavitating tip vortex, the eddy

viscosity drops below the surrounding values observed in the tip vortices with SST $k - \omega$ EARSM. The $k - \varepsilon$ model predicts significantly larger eddy viscosity in the slipstream. This behaviour smooths the details observable in the results obtained with the non-linear model, also causing the vapour to diminish in the tip vortices after having extended approximately to the hub cap in the downstream direction. Contrary to the SST $k - \omega$ EARSM, eddy viscosity is significant also in the cavitating hub vortex with the $k - \varepsilon$ model.

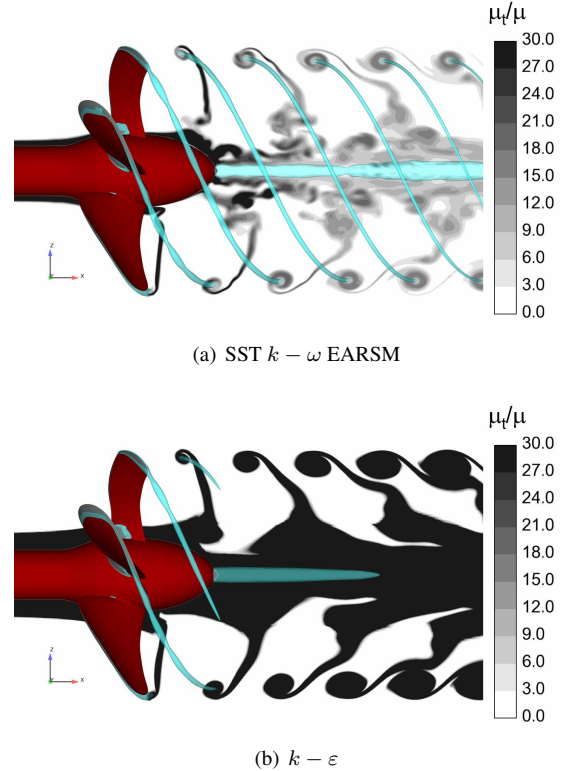


Figure 13: Non-dimensional eddy viscosity on the cut plane $y = 0$ utilizing different turbulence models. Cavitating conditions. The transparent iso-surface of the void fraction $\alpha = 0.1$ is colored by blue.

The flow field is visualized at the suction side of the blade and in the wake by the iso-surface of the magnitude of the vorticity vector $|\Omega_i| = 1.5 \times 10^3$ 1/s. in Fig. 14. The isosurface is colored by helicity $H = u_{i,r} \Omega_i / (|u_{i,r}| |\Omega_i|)$, where $u_{i,r}$ is the relative velocity vector in the rotating reference frame. The helicity denotes the cosine of the angle between the relative velocity and the absolute vorticity vectors, and tends to ± 1 in the vortex cores, the sign indicating the direction of swirl. In the figure, vortical structures are visualized at cavitating conditions. Minor instabilities are seen in the vorticity field near the sheet cavitation at the leading edge, but the re-entrant jet is directed up towards the cavitating tip vortex. The vapour in the sheet cavity is convected toward the cavitating tip vortex, and the sheet cavitation itself is stable. The root region

sheds unsteady flow structures in the wake. This was already inferable in the surface restricted streamlines in Fig. 10, for both utilized turbulence models. The rather stable root cavitation causes apparent changes to the flow geometry which lead to separation. Observing the results obtained with the non-linear model, the flow departing the trailing edge exhibits unsteadiness up to approximately $r/R = 0.5$. Separate vortex filaments form close to the surface of the hub shortly after the trailing edge of the blade with the SST $k - \omega$ EARSM. Utilizing the non-linear model, the vortical flow structures shed from the root region convect significantly longer and more detailed in the propeller wake. Similar phenomenon is observable for the cavitating hub vortex. The $k - \varepsilon$ model predicts slightly wider tip vortex region than the SST $k - \omega$ EARSM. The non-linear model then again produces significantly prolonged tip vorticity, along with the cavitating tip vortex (*cf.* Fig. 9). Dissipation is low in the tip vortex in the helical grid region with the SST $k - \omega$ EARSM.

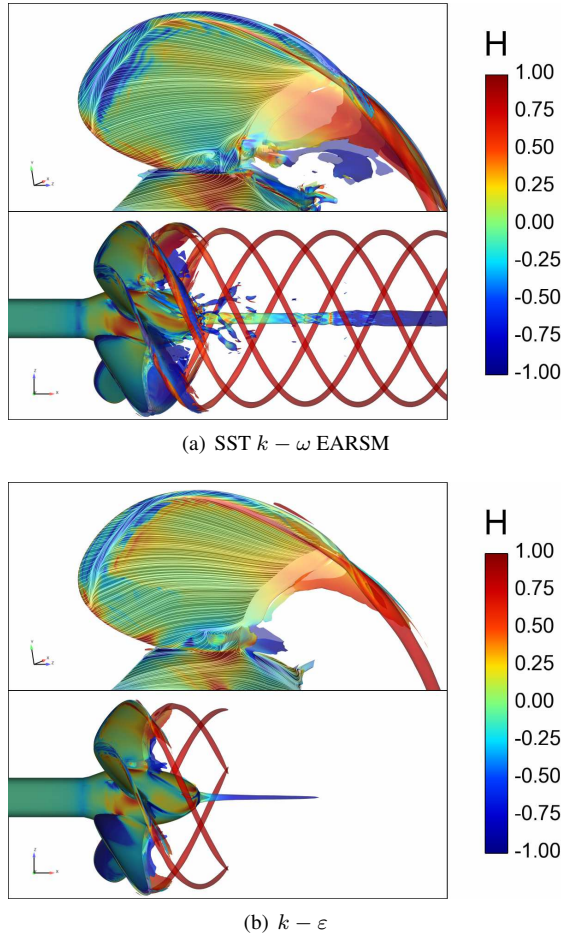


Figure 14: Iso-surface of the magnitude of the vorticity vector near the suction side with blade surface restricted streamlines (top), near the propeller and in the wake (bottom). The iso-surface is colored by helicity. Cavitating conditions.

5.4 Acoustic source distribution near the propeller

Fig. 15 shows the acoustic source terms obtained from the CFD solution on the cut plane $y = 0$ utilizing different turbulence models in wetted conditions. As shown by Saari- nen & Siikonen (2016), the divergence of the divergence of the Lighthill tensor, or the source term of the acoustic wave equation, can in incompressible cases be simplified to $\nabla \cdot (\nabla \cdot \tilde{T}_{ij}) = S_{inc} = -2\rho Q$ [kg/m³s²], where Q is the second invariant of the velocity gradient tensor. Fig. 15 shows results obtained with the different turbulence models.

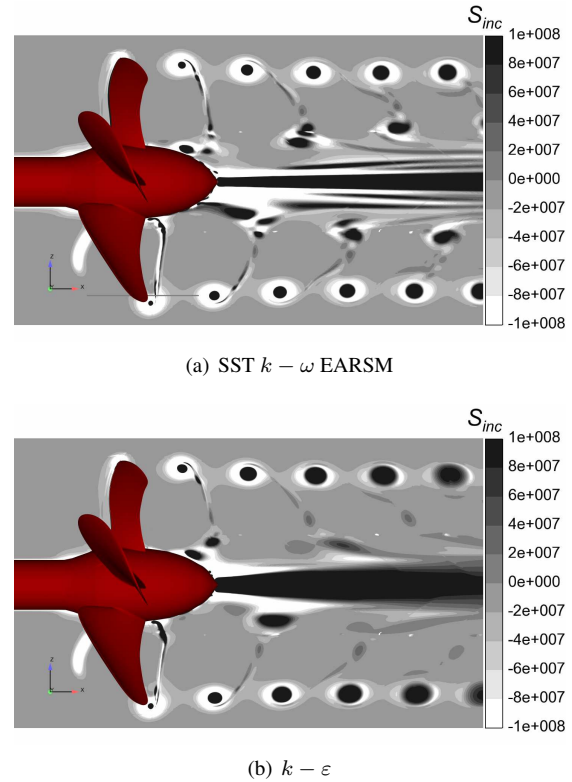


Figure 15: Acoustic source term distributions on the cut plane $y = 0$ utilizing different turbulence models. Wetted conditions.

It is seen that the sources created by the strong tip vortex are clearly predicted with both turbulence models. The tip vortices become slightly more pronounced and concentrated with the non-linear model. The tip vorticity remains strong although assumes a dissipative trend along the helix. The S_{inc} weakens more clearly in magnitude in the tip vortex region when utilizing the $k - \varepsilon$ model. The source strengths in the tip regions undergo relatively sharp variation in the surrounding outer regions of the tip vortex, where strain dominates over vorticity. There is a large difference in the source field behind the hub between the two turbulence models. The $k - \varepsilon$ model predicts more uniform and smooth wake, whereas there is more variation in the transverse direction with the SST $k - \omega$ EARSM. In addition, the S_{inc} distribution throughout the wake around $r/R \approx 0.4 \dots 0.5$, which is seemingly initiated by flow separation near the end

of the propeller hub, appears as more distinct in the results obtained with the non-linear model.

Fig. 16 shows a comparison of the acoustic source distributions predicted by the two different turbulence models for the cavitating conditions. The source term S_{inc} is approximated in the figure as the same as in an incompressible single-phase case. The application of different turbulence modelling has a significant influence on the source formation in the wake of the propeller. The source field in the slipstream of the $k - \varepsilon$ simulation appears as rather smooth and regular, whereas the source field obtained with the non-linear model exhibits apparent unsteadiness and significantly more detailed structures. This was hinted also in Figs. 13 and 14. The flow separation causes the above observations. Overall, the application of the non-linear turbulence closure produces vastly more pronounced flow structures along the propeller wake. The source strengths in the tip vortex region predicted by the $k - \varepsilon$ model seem to be more uniform compared to the SST $k - \omega$ EARSM. The non-linear turbulence model concentrates positive source region near the tip vortex core that is surrounded by a negative source region, where strain dominates over vorticity.

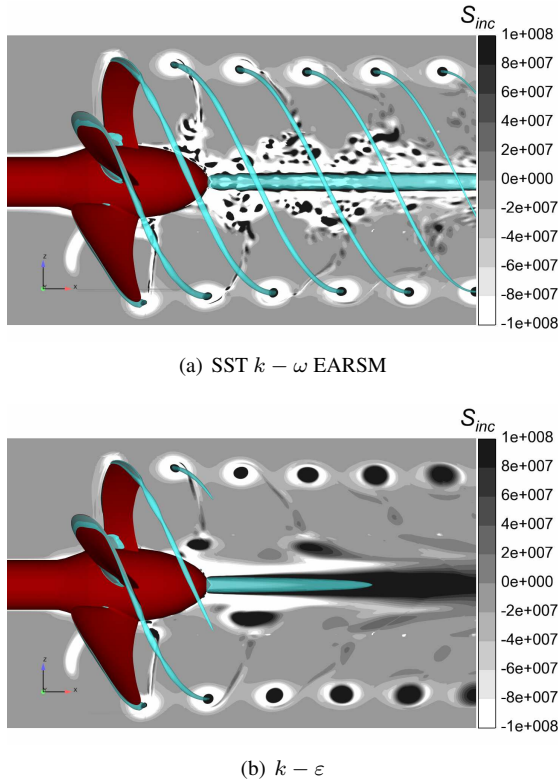


Figure 16: Acoustic source term distributions on the cut plane $y = 0$. Cavitating conditions. The transparent iso-surface of the void fraction $\alpha = 0.1$ is colored by blue.

5.5 Acoustic emission

A comparison of the mean square pressure inside the cavitation tunnel in wetted and cavitating conditions is shown in Fig.

17. Additionally, the figure shows a corresponding comparison of the mean square pressure at the ten first blade passing frequencies. The emission is the greatest at the propeller rate of revolution in all investigated cases. It is seen that in all computed cases significant noise emission is produced at the blade passing frequency and its harmonics. The difference of 10 – 15 dB between the f_{bpf} and its second harmonic is observed in wetted and cavitating results, depending upon the utilized turbulence closure. The greatest difference is obtained with the non-linear model in cavitating conditions. Cavitation results in clearly higher mean square pressure levels at frequencies close to the first two blade passing frequencies when utilizing the non-linear turbulence model. The mean square pressure reside at significantly higher levels for frequencies other than the f_{bpf} , up to approximately 1 kHz ($f/f_{bpf} = 10$) in the computations with the SST $k - \omega$ EARSM. Additionally, the mean square pressure levels at the blade passing frequency are slightly higher throughout the resolved frequency range when using the non-linear turbulence model. The wetted and cavitating results obtained using the $k - \varepsilon$ model show overall similar trend throughout the resolved frequency range, with notable increase in the cavitating conditions at the lower frequencies, other than f_{bpf} or its harmonics. An increase in the predicted mean pressure levels is visible at around 2.7 kHz ($f/f_{bpf} = 27$) in the cavitating case. This appears nearly similar in the results obtained with both utilized turbulence models. The observed behaviour is due to the fact that an unsymmetrical tunnel mode is excited, and this phenomenon is discussed by Hynninen *et al.* (2017).

Visualizations of the frequency domain pressure amplitudes at 100 Hz are given in Figs. 18 and 19 for wetted and cavitating conditions, respectively. The underlying transient CFD solutions have been obtained using the different turbulence models. A characteristic tube-like shape is initiated for all five blades in both wetted cases. In the cavitating conditions, the tubes seem to curl around the LE to the TE side, and partially come into contact with the tunnel walls. In the cavitating conditions the propeller also seems to emit a radially directed structure, which is rather similar between the turbulence models. In the wetted conditions, this structure appears as more longitudinally oriented. In the cavitating conditions, the effects of the different turbulence model to the details observable on the propeller wake are clear; *cf.* Fig. 16.

5.6 Comparison of acoustic emission of transient and quasi-steady CFD simulations

A comparison of the mean square pressure inside the cavitation tunnel between the transient and quasi-steady CFD solutions, in wetted and cavitating conditions, is shown in Fig. 20. Additionally, the figure shows a corresponding comparison of the mean square pressure at the ten first blade passing frequencies. The CFD results have been obtained utilizing the $k - \varepsilon$ turbulence model. Note that the transient CFD solutions obtained with $k - \varepsilon$ corresponds to the same CHA results as those already shown in Fig. 17. These are shown here again

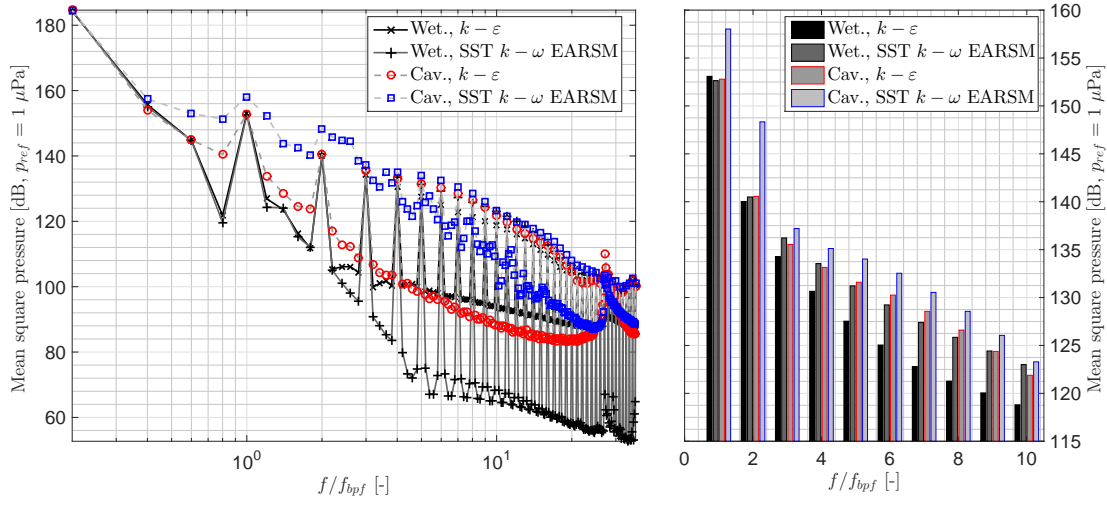


Figure 17: Mean square pressure inside the cavitation tunnel. The left figure depicts the whole resolved frequency range, and the right figure depicts the ten first BPFs. The x -axes have been normalized with the blade passing frequency.

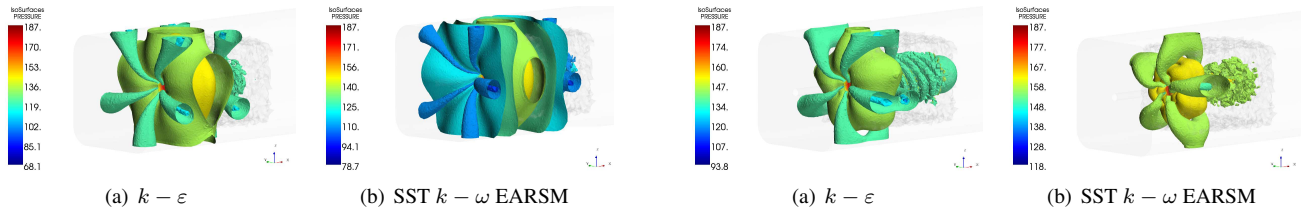


Figure 18: Visualizations of frequency domain pressures [dB, $p_{ref} = 1\mu\text{Pa}$] inside the cavitation tunnel at 100 Hz. Wetted conditions.

Figure 19: Visualizations of frequency domain pressures [dB, $p_{ref} = 1\mu\text{Pa}$] inside the cavitation tunnel at 100 Hz. Cavitating conditions.

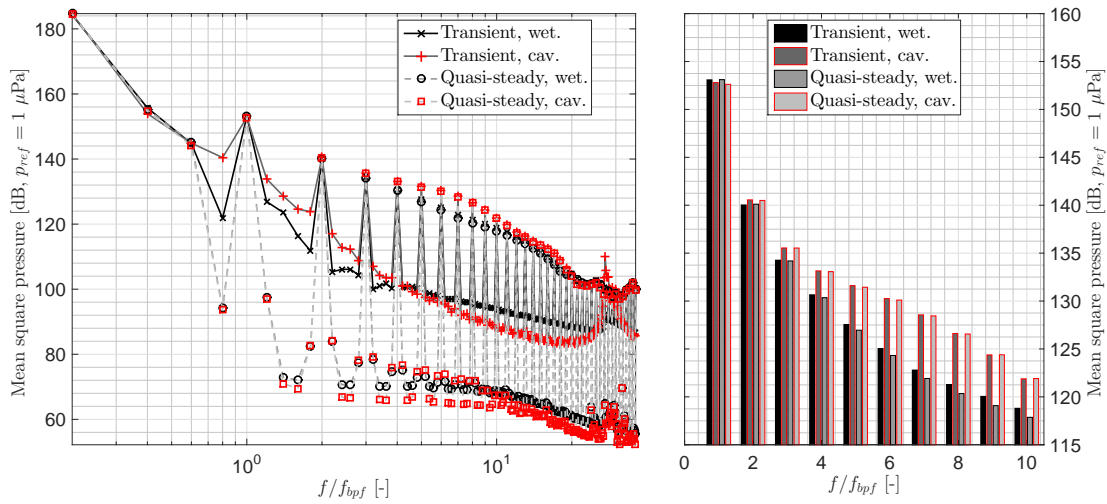


Figure 20: Mean square pressure inside the cavitation tunnel. The left figure depicts the whole resolved frequency range, and the right figure depicts the ten first BPFs. The x -axes have been normalized with the blade passing frequency.

for clarity of comparison. The emission is the greatest at the propeller rate of revolution for all investigated cases. The results from the two CFD solution strategies give comparable mean square pressure levels at the two first blade passing frequencies. This is observed in wetted and cavitating conditions. From the third harmonic onwards in the wetted case, the quasi-steady approximation yields a slightly more rapidly decreasing trend for the mean square pressure than is observed from the transient CFD results. For the cavitating case, the higher BPF harmonics show little difference between the transient and quasi-steady CFD results. At frequencies other than the harmonics of the f_{bpf} , the quasi-steady CFD results are significantly below those of from the transient CFD simulations from 80 Hz onwards. This is observed both in wetted and cavitating conditions. As is also seen in Fig. 17, the transient cavitating simulations provide enough high-frequency excitation for the eigenfrequencies of the numerical cavitation tunnel to appear in the computed mean square pressure representation. Fig. 20 shows that the quasi-steady approximation in the CFD solution does not yield ‘high-frequency’ content intense enough to result in similar phenomenon.

6 CONCLUSIONS AND FUTURE WORK

CFD and CHA simulations have been conducted for the PPTC propeller for one operating point in wetted and cavitating conditions. Good agreement between EFD and CFD has been achieved for the global forces in wetted and cavitating conditions. Excellent agreement with the cavitation tunnel tests has been achieved with regard to the prediction of the tip vortex cavitation.

In the propeller noise simulations, a two-step hybrid approach was used. Comparison of CFD results to corresponding CHA simulations indicate that the predicted noise emissions are reasonable. Effects due to different turbulence closures or due to cavitation can be recognized. It is seen that the propeller wake can act as an acoustic source on a wide frequency range, while cavitating tip vortex enhances the tonal signature considerably. However, validation of the present acoustic simulations with experimental results is still needed.

The comparison of single-point measurements conducted in a cavitation tunnel and the acoustic simulations is not straightforward. Sound pressure can be very sensitive to the location of the investigation point in the propeller near-field. The sound field characteristics in a wave guide, such as a cavitation tunnel, depend considerably on the type of the source, in addition to its position and orientation. The transformation of the results to corresponding free-field values is difficult. These issues are thoroughly discussed by Hynninen *et al.* (2017).

Cavitation contributes significantly to the acoustic emission due to the source term related to the density variations. This is visible in the results obtained with the non-linear turbulence model in wetted and cavitating conditions, where a clear difference is observed. Similar difference is not observed with the $k - \varepsilon$ turbulence model. Furthermore, in order to cap-

ture the possible broadband contribution due to the rapidly varying cavities, special attention is needed for the cavitation modelling. Current practice is to use a mass-transfer model based on $p - p_{sat}$, on its square root or other similar relation. One option to improve the cavitation modelling would be a multi-scale two-phase flow model, such as that developed by Hsiao *et al.* (2017).

Two different turbulence models were used within this study. The global propeller forces and flow phenomena including cavitation extent close to the blade were similar between the utilized turbulence models. The preliminary results shown indicate that the emission at the BPF and its first 2 – 3 multiples could be qualitatively captured even with quasi-steady RANS. However, the used turbulence model can have a significant influence especially to the flow field in the wake of the propeller and to the resulting simulated noise emission. The turbulence models can predict the wake of the propeller unphysically smooth or severely deteriorate the prediction of cavitation patterns in the wake, even though a fine computational grid is utilized. In this paper, the corresponding differences in the evaluation of the acoustic signature between the two eddy viscosity models were shown to be striking.

Utilizing URANS in conjunction with the Lighthill analogy, the sole coupling between the flow and acoustic solutions is the unsteady velocity vector. This, of course, does not include the fluctuating velocity, only the filtered time-dependent velocity. The possible broadband and high-frequency content of the acoustic signature can be completely lost when using an unsuitable turbulence closure for the acoustic source term evaluation. As was mentioned above, in cases where swift temporal and spatial variation of different types of cavities is expected, attention should be paid upon the cavitation modelling as well. For these reasons, two-phase DDES in connection with Roe’s SUPERBEE flux limiter for the convection of the void fraction will be utilized in a future study to gain additional insight.

A grid dependency study for the acoustic analyses is needed. In addition to evaluating the CFD sources from coarser and finer grids for the CHA, the sensitivity of the predicted noise levels to the numerical approximation used in the FEM should be investigated. To capture a more realistic flow solution for smaller turbulent fluctuations and possible cavity instabilities, a finer temporal resolution could be utilized in the present CFD solution.

ACKNOWLEDGEMENTS

The authors would like to express their gratitude for the support granted by the Finnish Funding Agency for Innovation (TEKES) and the German Federal Ministry for Economic Affairs and Energy within the ERA-NET MARTEC project ‘‘PropNoise’’. Without the funding the research project could not have been realized. The authors are also grateful to Dr. Otto Puolakka, Dr. Jerzy Matusiak and M.Sc. Tuomas Turunen for particularly fruitful discussions throughout this research.

REFERENCES

- Andrew, R. K., How, B. M., Mercer, J. A., & Dzieciuch, M. A. 2002. Ocean ambient sound: comparing the 1960s with the 1990s for a receiver off the California coast. Acoust. Res. Lett. Online, **3**.
- Balaras, E., Schroeder, S., & Posa, A. 2015. Large-eddy simulations of submarine propellers. J. Ship Res., **59**(4), 227–237.
- Barkmann, U., Heinke, H.-J., & Lübke, L. 2011. Potsdam propeller test case (PPTC). Test case description. *In: Second International Symposium on Marine Propulsors (smp'11). Workshop: Propeller performance.* Hamburg, Germany
- Budich, B., Schmidt, S. J., & Adams, N. A. 2015. Numerical investigation of a cavitating model propeller including compressible shock wave dynamics. *In: Fourth International Symposium on Marine Propulsors (smp'15).* Austin, Texas, USA
- Chase, N., & Carrica, P. M. 2013. Submarine propeller computations and application to self-propulsion of DARPA Suboff. Ocean Engineering, **60**, 68–80.
- Chien, K.-Y. 1982. Predictions of channel and boundary-layer flows with a low-Reynolds-number turbulence model. AIAA Journal, **20**(1), 33 – 38.
- Free Field Technologies SA. 2015. *Actran 16.1 User Manual.* Free Field Technologies SA, MSC Software Belgium SA, Axis Park Louvain-la-Neuve 9 rue Emile Francqui, B-1435 Mont-Saint-Guibert, Belgium.
- Guilmineau, E., Deng, G., Leroyer, A., Queutey, P., Visonneau, M., & Wackers, J. 2015. Influence of the Turbulence Closures for the Wake Prediction of a Marine Propeller. *In: Fourth International Symposium on Marine Propulsors (smp'15).* Austin, Texas, USA
- Hellsten, A., & Laine, S. 2000. Explicit algebraic Reynolds-stress modelling in decelerating and separating flows. *AIAA Paper 2000-2313, Denver.*
- Hsiao, C.-T, Ma, J., & Chahine, G.L. 2017. Multiscale tow-phase flow modeling of sheet and cloud cavitation. Int. J. Multiphase Flow.
- Hynninen, A., Tanttari, J., Viitanen, V.M., & Sipilä, T. 2017. On predicting the sound from a cavitating marine propeller in a tunnel. *In: Fifth International Symposium on Marine Propulsors (smp'17).* Espoo, Finland
- Ianniello, S., Muscari, R., & Di Mascio, A. 2013. Ship underwater noise assessment by the acoustic analogy. Part I: nonlinear analysis of a marine propeller in a uniform flow. J. Mar. Sci. Technol., **18**, 547 – 570.
- Lidtko, A.K., Turnock, S.R., & Humphrey, V.F. 2015. Use of acoustic analogy for marine propeller noise characterisation. *In: Fourth International Symposium on Marine Propulsors (smp'15).* Austin, Texas, USA
- Lightelijn, J. T. 2007. Advantages of different propellers for minimising noise generation. *In: Adler, H. E. (ed), Proceedings of the 3rd International Ship Noise and Vibration Conference.* London, UK
- Lighthill, M.J. 1952. On sound generated aerodynamically. Proc. R. Soc. A, **211**.
- Lindstrom, P. J., & Mallard, W. G. 2005. *Eds., NIST Chemistry WebBook.* NIST Standard Reference Database Number 69, National Institute of Standards and Technology, Gaithersburg MD. <http://webbook.nist.gov>.
- Lloyd, T., Rijpkema, D., & van Wijngaarden, E. 2015. Marine propeller acoustic modelling: comparing CFD results with an acoustic analogy method. *In: Fourth International Symposium on Marine Propulsors (smp'15).* Austin, Texas, USA
- Lu, N.-X., Bensow, R. E., & Bark, G. 2014. Large eddy simulation of cavitation development on highly skewed propellers. J. Mar. Sci. Technol.
- Mach, K.-P. 2011. Potsdam Propeller Test Case (PPTC). LDV velocity measurements with the model propeller VP1304. *SVA Potsdam Model Basin Report No.3754.* 32 p.
- Menter, F. 1994. Two-equation eddy-viscosity turbulence models for engineering applications. AIAA Journal, **32**(8), 1598 – 1605.
- Merkle, C.L., Feng, J., & Buelow, P.O.E. 1998. Computational modeling of the dynamics of sheet cavitation. *In: 3rd International symposium on cavitation* Grenoble, France, pp. 47-54.
- Miettinen, A., & Siikonen, T. 2015. Application of pressure- and density-based methods for different flow speeds. Int. J. Numer. Meth. Fluids, **79**(5), 243–267.
- Mitson, R.B. 1995. *Underwater noise from research vessels - review and recommendations.* Cooperative Research Report No. 209, International Council for the Exploration of the Sea.
- Muscari, R., Di Mascio, A., & Verzicco, R. 2013. Modeling of vortex dynamics in the wake of a marine propeller. Comp. Fluids, **73**, 65–79.
- Payne, R.S., & Webb, D. 1971. Orientation by means of long-range acoustic signaling in baleen whales. *Pages 110–141 of: Adler, H. E. (ed), Orientation: Sensory basis.* Ann. N.Y. Acad. Sci.
- Roe, P.L. 1985. Large scale computations in fluid mechanics. *In: Lectures in Applied Mathematics. Vol. 22.*

- Saarinen, P., & Siikonen, T. 2016. Simulation of HVAC flow noise sources with an exit vent as an example. Int. J. Ventilation, **15**(1), 45–66.
- Siikonen, T. 2009. *Developments of the cavitation model of the FINFLO code. Technical report F-44*. Finflo Ltd.
- Sipilä, T. 2012. *RANS analyses of cavitating propeller flows*. Licentiate Thesis, Aalto University.
- Sipilä, T.P., Sánchez-Caja, A., & Siikonen, T.L. 2014. Eddy vorticity in cavitating tip vortices modelled by different turbulence models using the RANS approach. *In: 6th European Conference on Computational Fluid Dynamics (ECFD VI)*. Barcelona, Spain
- Sipilä, T., Siikonen, T., Saisto, I., Martio, J., & Reksoprodjo, H. 2009. Cavitating propeller flows predicted by RANS solver with structured grid and small Reynolds number turbulence model approach. *In: Proceedings of the 7th International Symposium on Cavitation CAV2009*, Ann Arbor, USA .
- Sánchez-Caja, A., Rautahaimo, P., Salminen, E., & Siikonen, T. 1999. Computation of the incompressible viscous flow around a tractor thruster using a sliding mesh technique. *In: 7th International Conference in Numerical Ship Hydrodynamics*. Nantes, France
- Turunen, T., Siikonen, T., Lundberg, J., & Bensow, R. 2014. Open-water computations of a marine propeller using Open-FOAM. *In: 6th European Conference on Computational Fluid Dynamics (ECFD VI)*. Barcelona, Spain
- van Albada, G.D., van Leer, B., & Roberts, W.W. 1982. A comparative study of computational methods in cosmic gas dynamics. Astronomy and Astrophysics, **108**(76), 76 – 84.
- Van Leer, B. 1979. Towards the ultimate conservative difference scheme. V. A second-order sequel to Godunov's method. J. Comp. Phys., **32**(1), 101–136.
- Viitanen, V., Martio, J., & Sipilä, T. 2015. FINFLO two-phase URANS predictions of propeller performance in oblique flow. *In: Fourth International Symposium on Marine Propulsors (smp'15)*. Workshop: Propeller performance. Austin, Texas, USA
- Wallin, S., & Johansson, A. 2000. A complete explicit algebraic Reynolds stress model for incompressible and compressible turbulent flows. J. Fluid Mech., 89 – 132.
- Curle, N. 1955. The influence of solid boundaries upon aerodynamic sound. Proc. R. Soc. A, 231:505–514
- Ffowcs-Williams, J.E. and Hawkins, D.L. 1969. Sound generation by turbulence and surfaces in arbitrary motion. Phil. Trans. R. Soc. A, 264:321–342
- Caro, S. Sandboge, R. Iyer, J. and Nishio, Y. 2007. Presentation of a CAA formulation based on Lighthill's analogy for fan noise. Proc. of the Conference on Fan Noise, 17–19. Lyon, France
- Oberai, A.A. Roknaldin, F. and Hughes, T.J.R. 2000. Computational procedures for determining structural-acoustic response due to hydrodynamic sources. Comput. Methods in Appl. Mech. Eng., 190:345–361
- Viitanen, V.M., Siikonen, T. 2017. Numerical simulation of cavitating marine propeller flows. *In: B.H. Skallerud & H.I. Andersson (ed.): MekIT'17 - Ninth national conference on Computational Mechanics*. International Center for Numerical Methods in Engineering (CIMNE), pp. 385–409. Trondheim, Norway. ISBN: 978-84-947311-1-2

DISCUSSION

Question from Thomas Lloyd

Why did you choose this acoustic model? Why not FW-H? The acoustic sources in the wake are well resolved by EARSIM, but they are quadrupole type – how important are they for the overall noise? There is little difference in the dB level between $k - \varepsilon$ and EARSIM for wetted flow.

Authors' closure

Thank you for the questions, and for the interest toward our work. We utilized the Lighthill analogy with the density as the primary variable. The inhomogeneous wave equation for the density perturbations is solved using an acoustic FE method, which relies on the CFD solution with regard to the sound generation.

In the integral methods, such as those introduced by Curle (1955) or Ffowcs-Williams & Hawkins (1969), a drawback is that the propagation resolution is only valid for external problems, where the free-field assumption is acceptable. In practical problems, this may not be valid, and the presence of solid walls can significantly impact the acoustic waves (Caro *et al.*, 2007). The effect of the solid boundaries must, then, be explicitly incorporated within the surface integrals, *i.e.*, requiring *a priori* knowledge of hard wall Green's function (Oberai *et al.*, 2000). These are usually not known for complex geometries. In contrast to the integral methods, when using the weak formulation of the Lighthill's analogy, Eq. (12), the effect of moving boundaries is naturally accounted for, and there are no limitations on the elasticity or geometry of the surrounding boundaries (Free Field Technologies SA, 2015). Moreover, in the acoustic solution we do not explicitly distinguish the different types of sound sources, and we do not utilize the pressure provided by the CFD solution. Our approach on the other hand requires a discretization of the entire acoustic domain, which in this study was the cavitation tunnel.

In the simulated wetted case, flow separation near the blade

root or at the hub is not dramatic. Flow around the blades behaves quite smoothly in the wetted case with no marked separation. In Fig. 15 we see contribution mainly due to the tip vortices, hub vortex, blade trailing edge, and minor instabilities which likely originate from small separation region near the blade root at TE. Most dominant effects (that are resolvable by URANS) occur at the BPF, which is evident in the results of acoustic computations as well. The acoustic emission is relatively similar between the utilized turbulence closures up to the third BPF (see Fig. 17).

Then again in the cavitating case, the computations predict also a rather stable root cavitation, which causes apparent changes to the flow geometry that lead to separation near the TE. We observed in Figs. 12, 14 and 16 that this introduces instabilities in the wake as well, more prominent than in the wetted case. The application of the $k - \varepsilon$ turbulence model resulted in an over prediction of the eddy viscosity levels in the wake of the propeller. This behaviour tends to smooth the instabilities caused by the separation, and attenuate also the broadband noise signature. EARSM typically dissipates

less the wake field, allowing a more dynamic behaviour of the flow and cavities. Consequently, an increased level of broadband noise can be resolved. In a recent study, Viitanen & Siikonen (2017) further assessed several different turbulence modelling approaches including delayed detached eddy simulation (DDES) for the predictions of cavitating flow over the PPTC propeller.

Question from Johan Bosschers

Where are the monitoring points for the acoustic pressures located?

Authors' closure

Thank you for the remark. The sensitivity of the sound pressure can be very high with respect to the location of an investigation point near the source, especially for a propeller that incorporates multiple types of elementary noise sources (monopoles, dipoles, quadrupoles). Hence, we characterized the sound emission using a volumetric mean square pressure inside the cavitation tunnel.